**Wind and Structures**, *Vol. 31, No. 3 (2020) 255-267*
DOI: https://doi.org/10.12989/was.2020.31.3.255


# Wind loading of a finite prism: aspect ratio, incidence and boundary layer thickness effects

Herman Heng[a] and David Sumner*

*Department of Mechanical Engineering, University of Saskatchewan, 57 Campus Drive, Saskatoon, Saskatchewan, S7N 5A9, Canada*

(*Received September 5, 2019, Revised January 13, 2020, Accepted March 9, 2020*)

**Abstract.** A systematic set of low-speed wind tunnel experiments was performed at Re = $6.5\times10^4$ and $1.1\times10^5$ to study the mean wind loading experienced by surface-mounted finite-height square prisms for different aspect ratios, incidence angles, and boundary layer thicknesses. The aspect ratio of the prism was varied from AR = 1 to 11 in small increments and the incidence angle was changed from $\alpha = 0°$ to 45° in increments of 1°. Two different boundary layer thicknesses were used: a thin boundary layer with $\delta/D = 0.8$ and a thick boundary layer with $\delta/D = 2.0$–2.2. The mean drag and lift coefficients were strong functions of AR, $\alpha$, and $\delta/D$, while the Strouhal number was mostly influenced by $\alpha$. The critical incidence angle, at which the prism experiences minimum drag, maximum lift, and highest vortex shedding frequency, increased with AR, converged to a value of $\alpha_c = 18° \pm 2°$ once AR was sufficiently high, and was relatively insensitive to changes in $\delta/D$. A local maximum value of mean drag coefficient was identified for higher-AR prisms at low $\alpha$. The overall behaviour of the force coefficients and Strouhal number with AR suggests the possibility of three flow regimes.

**Keywords:** bluff body; surface-mounted finite-height square prism; wind loading; vortex shedding; drag coefficient; lift coefficient; critical incidence angle

## 1. Introduction

Flow around a surface-mounted finite-height square prism (of width $D$ and height $H$, Fig. 1) is a fundamental three-dimensional (3D) bluff-body shape that may be representative of flow around slender buildings or short block-shaped electronic components on circuit boards. The interaction between the prism and the boundary layer on the ground plane (with freestream velocity $U_\infty$, mean streamwise velocity profile $u(z)$, and boundary layer thickness $\delta$), plus the flow around the free end of the prism, create a complex 3D flow field that differs considerably from that of the familiar "infinite" (or two-dimensional, 2D) square prism.

Reynolds number (Re = $U_\infty D/\nu$, where $\nu$ is the fluid's kinematic viscosity) effects have not been extensively studied for finite prisms, but see McClean and Sumner (2014), Wang *et al*. (2017), Zhang *et al*. (2017), Sohankar *et al*. (2018), and Wang (2019) for some details. The effect of AR has been considered in a wide range of studies; prisms that are below a critical value of aspect ratio have a unique wake structure where familiar antisymmetric Kármán vortex shedding is absent (Sakamoto and Arie 1983, Sakamoto and Oiwake 1984, Sakamoto 1985, Wang *et al*. 2009, Wang and Zhou 2009, Saha 2013, McClean and Sumner 2014, Porteous *et al*. 2017, Sumner *et al*. 2017, Unnikrishnan *et al*. 2017, Zhang *et al*. 2017, Yauwenas *et al*. 2019). The thickness of the ground plane's boundary layer also affects the wake (Wang *et al*. 2006, Hosseini *et al*. 2013, El Hassan *et al*. 2015, Wang *et al*. 2017, Behera and Saha 2019).

Four main flow patterns have been identified for the 2D square prism at different $\alpha$ (Fig. 2). The relative positions of the four corners or vertical edges (labeled 'a', 'b', 'c', and 'd' in Figs. 1 and 2), the behaviour of the separated shear layers from corners 'a' and 'd', and the tendency for shear layer reattachment onto side 'c-d', are vital for determining the wind loading and vortex shedding. The critical incidence angle $\alpha_c$ corresponds to orientation where the lower shear layer first reattaches onto the lower side ('d-c') at vertical edge 'c', and thus marks the boundary between the perfect separation (asymmetric) (Fig. 2(b)) and reattachment (Fig. 2(c)) flow patterns.

For surface-mounted finite-height prisms, the incidence angle ranges for these four flow patterns, how and if they might vary along the prism height, and whether other flow patterns may occur, have not yet been broadly investigated. Incidence angle effects for wide ranges of Re, AR, and $\delta/D$ are generally not well understood since most studies of finite prisms have been limited to $\alpha = 0°$ where the prism face is normal to the oncoming flow. Only a small number of studies have focused on combinations of Re, AR, $\delta/D$, and $\alpha$ (where the four main parameters are systematically varied over large ranges and with small increments) on the flow field (Unnikrishnan *et al*. 2017, Cao *et al*. 2019), windloading (Sakamoto and Oiwake 1984, McClean and Sumner 2014), pressure distribution (Lim 2009, Lee *et al*. 2016), or vortex shedding (Sakamoto 1985, McClean and

*Corresponding author, Professor
E-mail: david.sumner@usask.ca
[a]M.Sc. Student
E-mail: cloud.heng@usask.ca


http://www.techno-press.com/journals/was&subpage=7

ISSN: 1226-6116 (Print), 1598-6225 (Online)

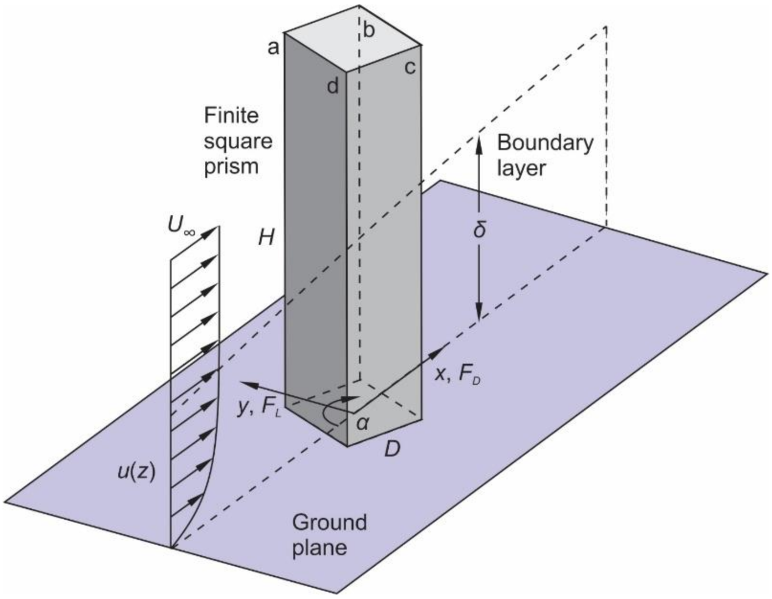


Fig. 1 Schematic of flow around a surface-mounted finite-height square prism (of height $H$ and width $D$) immersed in a flat-plate boundary layer (with thickness $\delta$, mean velocity profile $u(z)$, vertical coordinate $z$, and freestream velocity $U_\infty$). The incidence angle $\alpha$ has positive rotation in the CW direction. The drag force $F_D$ and lift force $F_L$ are aligned with the streamwise $x$ and cross-stream $y$ coordinate directions, respectively. The prism's vertical edges are labelled as 'a', 'b', 'c', and 'd'.

and Sumner 2014). To address this gap in the literature, the present experimental study examines the effects of changing AR, $\delta/D$, and $\alpha$ on the behaviour of mean drag force coefficient $C_D$, mean lift force coefficient $C_L$, and Strouhal number St. Finite prisms of AR = 1 to 11 (in increments of 0.5) were tested over $\alpha$ = 0° to 45° (in increments of 1°). The wind loading ($C_D$, $C_L$) measurements were made at Re = $1.1\times10^5$ for two boundary layer thicknesses of $\delta/D$ = 0.8 (representing a "thin" boundary layer) and $\delta/D$ = 2.0 (representing a "thick" boundary layer). Vortex shedding frequency measurements (to obtain St) were made at Re = $6.5\times10^4$ for $\delta/D$ = 0.8 and 2.2.

## 2. Literature review

### *2.1 Mean drag force coefficient*

For a 2D square prism at $\alpha$ = 0°, the mean drag coefficient ($C_D = F_D(½\rho U_\infty^2 DH)^{-1}$, where $F_D$ is the mean drag force and $\rho$ is the fluid's density) is relatively insensitive to Reynolds number from $10^3 < \mathrm{Re} < 10^6$ (Bai and Alam, 2018). The same behaviour has been observed for finite prisms. For example, Wang *et al*. (2017) performed an experimental investigation from $6.8\times10^4 \le \mathrm{Re} \le 6.12\times10^5$ and showed that $C_D$ did not vary significantly with Re (within this relatively limited range) for a finite height square prism with AR = 5 at $\alpha$ = 0°. At much lower Reynolds numbers, however, $C_D$ is much more sensitive to Re, as demonstrated by Zhang *et al*. (2017) in their simulation of the flow around a surface-mounted finite height square prism of AR = 4 at Re = 50 to 1000; this same sensitivity at low Re is also seen for the infinite (2D) square prism (Bai and Alam 2018).

For the finite prism, $C_D$ is always lower than that of the infinite prism owing to the effects of the 3D flow field. The effect of the aspect ratio (AR) at $\alpha$ = 0° has been experimentally investigated by Akins *et al*. (1977), Sarode *et al*. (1981), Sakamoto and Oiwake (1984), Sakamoto (1985), McClean and Sumner (2014) and numerically investigated by Saha (2013). Data from selected studies in Fig. 3(a) suggest three trends in the $C_D$ = f(AR) relationship: (i) $C_D$ tends to increase with AR at lower aspect ratios; (ii) $C_D$ becomes nearly independent of AR at intermediate aspect ratios; and (iii) $C_D$ begins to slowly increase with AR at higher aspect ratios. Similar trends have been reported for the $C_D$ of finite cylinders (Beitel, Heng, and Sumner, 2019) and the overall sound pressure level of finite prisms (Moreau and Doolan 2013).

The variation of $C_D$ with the incidence angle ($\alpha$) is shown in Fig. 4(a). The sensitivity of $C_D$ to $\alpha$ for the finite prism is more subdued compared to the 2D prism, but the general trends for the finite prism are similar, with a minimum $C_D$ occurring at the critical incidence angle $\alpha_c$. For the finite prism, $\alpha_c$ is sensitive to aspect ratio and is higher than that of the infinite (2D) prism.

Sakamoto (1985) is one of the few studies to consider boundary layer thickness effects, for AR = 2, 3, 4, 5 at $\alpha$ = 0° only. He found that for all aspect ratios, $C_D$ increased linearly with $H/\delta$, i.e. a thicker boundary layer (relative to $H$) resulted in smaller $C_D$. The same observation was made by Sakamoto and Oiwake (1984) and Wang *et al*. (2017) and is consistent with the behaviour of finite cylinders (Beitel *et al*. 2019).

### *2.2 Mean lift force coefficient*

A mean lift force is experienced by square prisms for

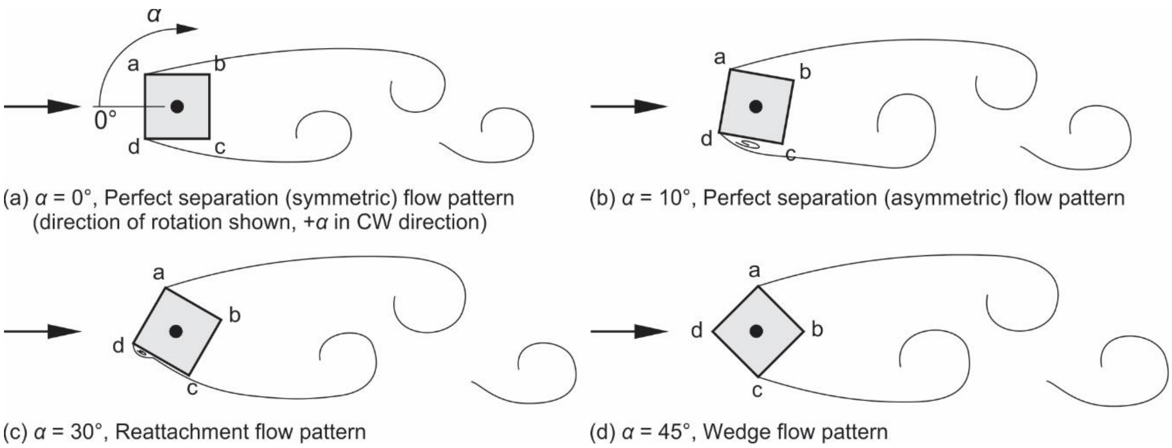


Fig. 2 Schematics of the four flow patterns for a 2D square prism at Re ≈ $10^4$ based on the classification of Igarashi (1984): (a) perfect separation (symmetric) flow pattern, shown for $\alpha$ = 0°, (b) perfect separation (asymmetric) flow pattern, shown for $\alpha$ = 10°, (c) reattachment flow pattern, shown for $\alpha$ = 30°, (d) wedge flow pattern, shown for $\alpha$ = 45°. Note the locations of the four corners or vertical edges, 'a', 'b', 'c', 'd', and the CW direction of increasing incidence angle (see also Fig. 1).

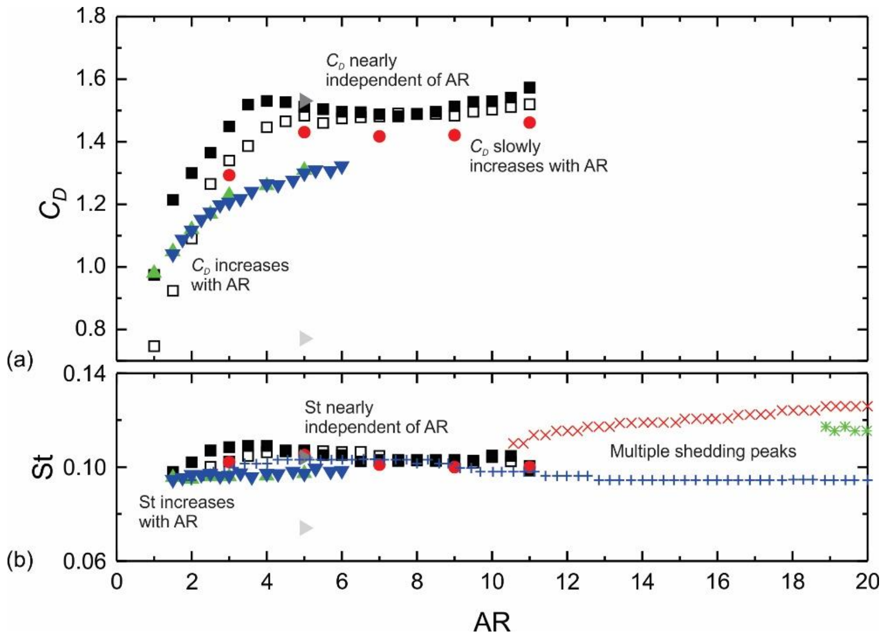


Fig. 3. Published experimental data for a surface-mounted finite-height square prism at $\alpha$ = 0° illustrating the dependence of the (a) mean drag coefficient and (b) Strouhal number on the prism's aspect ratio. ▼, Sakamoto and Oiwake (1984), Re = $2.82\times10^4$ to $1.1\times10^5$, $\delta/D$ = 1.0 to 4.0; ▲, Sakamoto (1985), Re = $3.5\times10^4$ to $1.8\times10^5$, $\delta/D$ = 0.67 to 3.33; ●, McClean and Sumner (2014), Re = $7.3\times10^4$, $\delta/D$ = 1.5; +, Porteous *et al.* (2017), frequency peak P1, Re = $1.4\times10^4$, $\delta/D$ = 1.3; ×, Porteous *et al.* (2017), frequency peak P2, Re = $1.4\times10^4$, $\delta/D$ = 1.3; ✳, Porteous *et al.* (2017), frequency peak P3, Re = $1.4\times10^4$, $\delta/D$ = 1.3; ▶, Wang *et al.* (2017), Re = $1.1\times10^5$, $\delta/D$ = 1; ▷, Wang *et al.* (2017), Re = $1.1\times10^5$, $\delta/D$ = 7; ■, present study, Re = $1.1\times10^5$ ($C_D$ data) and Re = $6.5\times10^4$ (St data), $\delta/D$ = 0.8; □, present study, Re = $1.1\times10^5$, $\delta/D$ = 2.0 ($C_D$ data) and Re = $6.5\times10^4$, $\delta/D$ = 2.2 (St data).

angles between $\alpha$ = 0° and 45°. The mean lift coefficient ($C_L = F_L(½\rho U_\infty^2 DH)^{-1}$, where $F_L$ is the mean lift force) is strongly sensitive to $\alpha$, and for the case of the finite prism, is also a complex function of AR (Fig. 4(b)). Based on the CW rotation of the prism (Figs. 1 and 2), the lift force is almost always induced in the $-y$ direction, towards side 'c-d' where shear layer reattachment ultimately occurs, and therefore $C_L$ has a negative value.

An increase in AR tends to result in an increase in the $C_L$ magnitude (i.e., $C_L$ becomes more negative) when $\alpha > \alpha_c$.

For very low aspect ratios, the lift coefficient attains a small positive value (directed in the $+y$ direction) between $\alpha$ = 20° and 45°, as shown in the data for AR = 1 from Sakamoto (1985) in Fig. 4(b). This feature has also been reported in some, but not all, studies of 2D square prisms at incidence.

For both infinite and finite prisms, $C_L$ attains its maximum (most negative) value at the critical incidence angle. For the finite prism, $\alpha_c$ tends to be higher than that of the infinite prism and increases with AR (Sakamoto 1985,

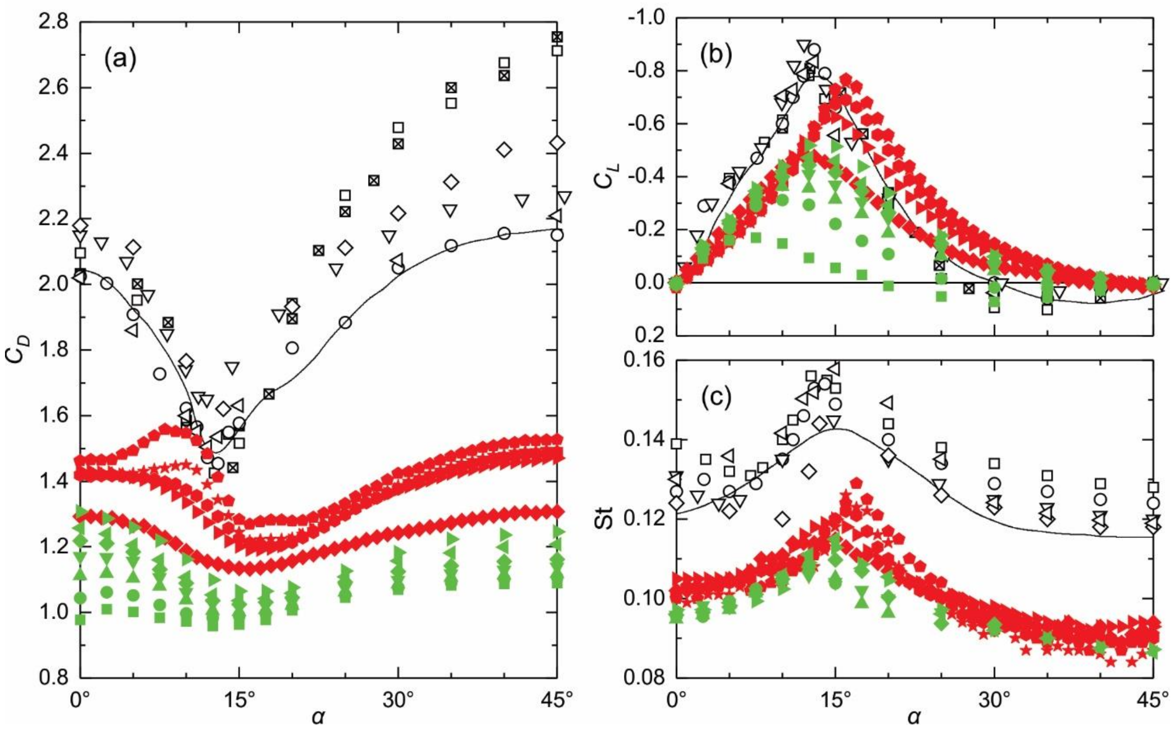

Fig. 4. Published experimental data for a finite square prism, at selected AR, illustrating the dependence of the (a) mean drag coefficient, (b) mean lift coefficient, and (c) Strouhal number on incidence angle. Data for the infinite (2D) prism are also included. Sakamoto (1985), Re = $3.5\times10^4$ to $1.8\times10^5$, $\delta/D$ = 0.67 to 3.33, green solid symbols: ■, AR = 1; ●, AR = 1.5; ▲, AR = 2; ▼, AR = 2.5 ◆, AR = 3; ◀, AR = 4; ▶, AR = 5. McClean and Sumner (2014), Re = $7.3\times10^4$, $\delta/D$ = 1.5. red solid symbols: ◆, AR = 3; ▶, AR = 5; ⬢, AR = 7; ★, AR = 9; ⬟, AR = 11. Infinite (2D) square prism: □, Igarashi (1984), Re = $3.7\times10^4$; ⊠, Igarashi (1984), Re = $5.6\times10^4$; ○, Knisely (1990), Re = $2.2\times10^4$ to $4.4\times10^4$; ▽, Norberg (1993), Re = $1.3\times10^4$; ◇, Obasaju (1983), Re = $4.74\times10^4$; ◁, Yen and Yang (2011), Re = $3.6\times10^4$; ——, Lee (1975), Re = $1.76\times10^5$, uniform flow.

McClean and Sumner 2014). Unnikrishnan *et al*. (2017) showed that the greatest asymmetry in the mean wake of a finite prism occurs at $\alpha_c$, while Sohankar *et al*. (2018) showed that the wake attains its minimum width at $\alpha_c$.

There are few studies of boundary layer thickness effects on $C_L$ and $\alpha_c$. Akins *et al*. (1977) adopted four boundary layers in their experiments, with the same thickness but with different wall shear stress or friction velocity. They discovered that the magnitude of $C_L$ decreased slightly when the friction velocity at the wall increased, regardless of AR.

### *2.3 Strouhal number*

Systematic investigations of the effects of AR on the Strouhal number (St = $fD/U_\infty$, where $f$ is the vortex shedding frequency) of a finite prism, for $\alpha$ = 0° only, have been reported by Sakamoto and Oiwake (1984), Sakamoto (1985), and Porteous *et al*. (2017). A compilation of St data at $\alpha$ = 0° in Fig. 3(b) show three basic trends: (i) at low aspect ratios, there is first an absence of a shedding peak followed by an increase in St with AR; (ii) at intermediate aspect ratios St tends to be independent of AR; (iii) at higher aspect ratios, multiple shedding peaks occur. Porteous *et al*. (2017) identified four distinct shedding regimes for the finite prism at $\alpha$ = 0°: regime R0 occurs for AR < 2, where a well-defined peak is not evident in the power spectrum; regime R1 occurs for 2 < AR < 10, where a single and relatively sharper peak (P1) is found; regime R2 occurs for 10 < AR < 18, where two shedding peaks (P1 and P2) are found; regime R3 occurs for AR > 18, where there is a third peak (P3).

Non-zero incidence angles strongly influence St (Fig. 4(c)) and a maximum value of St is found at $\alpha_c$. For the finite prism, systematic studies of the effects of both AR and $\alpha$ on the Strouhal number were performed by Sakamoto (1985) and McClean and Sumner (2014); results are shown in Fig. 4(c) for illustrative purposes; Sohankar *et al*. (2018) also considered the effects of $\alpha$ but for AR = 7 only.

The effect of the boundary layer thickness on vortex shedding at $\alpha$ = 0° was investigated by Sakamoto and Oiwake (1984), Wang *et al*. (2017), and Kindree, Shahroodi, and Martinuzzi (2018). Sakamoto and Oiwake (1984) studied the relationship between St and $H/\delta$ for a rectangular prism with AR = 3 and found that a thicker boundary layer results in slightly smaller vortex shedding frequency. A similar conclusion was reported by Wang *et al*. (2017) for a prism of AR = 5 with $\delta/D$ = 1 and 7. Kindree *et al*. (2018) used laminar, transitioning, and turbulent boundary layers but did not find an obvious shift in the vortex shedding frequency; however, they observed a low-frequency signature (with a value about ten times smaller than the shedding frequency) for the laminar and transitioning boundary layers.

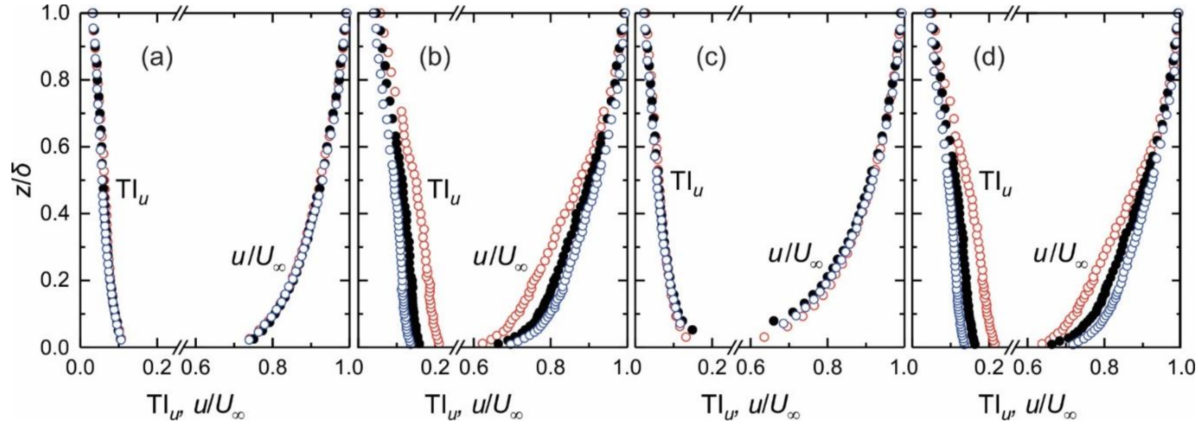


Fig. 5. Properties of the boundary layers, including the mean streamwise velocity and turbulence intensity profiles: (a) thin boundary layer, $U_\infty$ = 40 m/s (corresponding to Re = $1.1\times10^5$, $\delta/D$ = 0.8); (b) thick boundary layer, $U_\infty$ = 40 m/s (corresponding to Re = $1.1\times10^5$, $\delta/D$ = 2.0); (c) thin boundary layer, $U_\infty$ = 22.5 m/s (corresponding to Re = $6.5\times10^4$, $\delta/D$ = 0.8); (d) thick boundary layer, $U_\infty$ = 22.5 m/s (corresponding to Re = $6.5\times10^4$, $\delta/D$ = 2.2). ○, $x/D = -5$; ●, $x/D$ = 0; ○, $x/D$ = +5.

## 3. Experimental approach

The wind tunnel set-up and instrumentation were similar to Beitel *et al*. (2019). The dimensions of the wind tunnel test section were 0.91 m (height) × 1.13 m (width) × 1.96 m (length). A National Instruments PCIe-6259 16-bit data acquisition board was used with LabVIEW software to sample data at 1 kHz for 20 s. The flow conditions in the wind tunnel were measured with a United Sensor Pitot-static probe (with type-T thermocouple). The freestream dynamic pressure was measured with a Datametrics Barocel Type 590 differential pressure transducer and the freestream static pressure was measured with a Datametrics Barocel Type 600 absolute pressure transducer. Two different freestream velocities were used: (i) for the measurements of $F_D$ and $F_L$, a freestream velocity of $U_\infty$ = 40 m/s was used to increase the accuracy of the very small forces experienced by the shortest prisms, resulting in Re = $1.1\times10^5$; (ii) for the vortex shedding frequency measurements, $U_\infty$ = 22.5 m/s was used, primarily to keep the wind tunnel temperature as low as possible, resulting in Re = $6.5\times10^4$. These two Reynolds numbers are sufficiently close to one another that any Re effects are very small. For both freestream velocities, the streamwise freestream turbulence intensity was less than 0.6%.

The finite square prisms were manufactured from aluminium square tube in 21 different aspect ratios (AR = 1 to 11, with an increment of 0.5) with a common width of $D$ = 48 mm. Smooth surfaces and sharp edges were maintained on all the models. The range of AR is larger than those of all other studies with the exception of Porteous *et al*. (2017). The maximum solid blockage ratio was 2.6%. Each of the 21 prisms was rotated from $\alpha = 0°$ to 45° in increments of 1° so as to cover the four main flow patterns (Fig. 2) and provide the sufficient angular resolution to resolve $\alpha_c$.

The prism was mounted on a force balance to measure $F_D$ and $F_L$. The uncertainty in $C_D$ ranged from ± 0.18 for the prism of AR = 1 to ± 0.02 for the prism of AR = 11. The uncertainty in $C_L$ ranged from ± 0.09 for the prism of AR = 1 to ± 0.01 for the prism of AR = 11.

A Dantec Streamline constant-temperature anemometer and a 55P11 single-wire hot-wire probe were used to obtain the vortex shedding frequency. The probe was placed in a fixed position in the wake, at $x/D$ = 6, $y/D$ = 2.5, and $z/H$ = 0.5 (corresponding to the mid-height of the prism). The power spectrum of the voltage fluctuations was computed to determine the vortex shedding peak and corresponding frequency ($f$) with an estimated uncertainty of ± 2 Hz. The uncertainty in the Strouhal number (St) was ± 0.004.

The prisms were mounted normal to a ground plane with streamwise and cross-stream dimensions of 1790 mm × 1030 mm. With no trip installed, a "thin" fully developed turbulent flat-plate boundary layer with $\delta/D$ = 0.8 was present at the location of the prism. Installation of boundary layer trip near the leading edge of the ground plane resulted in a "thick" turbulent flat-plate boundary layer, with $\delta/D$ = 2.0 for the force measurements at $U_\infty$ = 40 m/s (Re = $1.1\times10^5$) and $\delta/D$ = 2.2 for the vortex shedding frequency measurements at $U_\infty$ = 22.5 m/s (Re = $6.5\times10^4$). The mean streamwise velocity ($u/U_\infty$) and turbulence intensity ($TI_u$) profiles for the boundary layers are shown in Fig. 5. The thick boundary layers were still developing at the location of the prism.

## 4. Results and discussion ($\alpha$ = 0°)

For the two Reynolds numbers used in the present experiments (Re = $1.1\times10^5$ and Re = $6.5\times10^4$), the mean drag coefficient and Strouhal numbers for the infinite (2D) square prisms at $\alpha$ = 0° are $C_D \approx 2.21$ and St ≈ 0.134 (Bai and Alam 2018). The values of $C_D$ and St for the surface-mounted finite-height square prisms are consistently lower for all aspect ratios and $\delta/D$ values.

### *4.1 Mean drag force coefficient*

Fig. 6(a) shows the behaviour of the mean drag coefficient with aspect ratio at $\alpha$ = 0° for both the thin ($\delta/D$

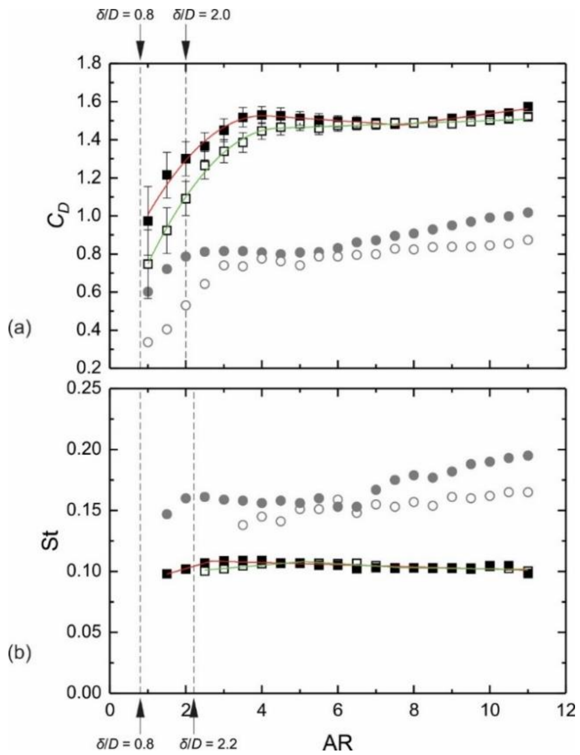


Fig. 6 Mean drag coefficient data (at Re = $1.1\times10^5$) (a) and Strouhal number data (at Re = $6.5\times10^4$) (b) as a function of aspect ratio (AR) for a finite square prism. Red and green curves show piecewise curve fits to the data (R-Squared value of 0.99 for both the thin and thick boundary layer $C_D$ data; R-Squared values of 0.76 and 0.83 for the thin and thick boundary layer St data, respectively). Finite square prism: ■, thin boundary layer ($\delta/D$ = 0.8); □, thick boundary layer ($\delta/D$ = 2.0 or 2.2). Finite cylinder, Re = $6.5\times10^4$ (Beitel *et al*. 2019): ●, thin boundary layer ($\delta/D$ = 0.6); ○, thick boundary layer ($\delta/D$ = 1.9).

= 0.8) and thick ($\delta/D$ = 2.0) boundary layers at a single Reynolds number of Re = $1.1\times10^5$. For the thin boundary layer, the same three general trends identified in Fig. 2(a) are seen. First, at low aspect ratios, where the prism is below the critical aspect ratio, $C_D$ increases rapidly with AR; the upper limit of the rapid increase in $C_D$ is AR ≈ 4. The finite-cylinder data shown in Fig. 6(a) exhibit a similar trend but the rapid increase in $C_D$ with AR ends sooner at AR ≈ 2.5. Second, at intermediate aspect ratios (4 ≤ AR ≤ 8), $C_D$ becomes nearly independent of AR, attaining a value of $C_D$ ≈ 1.50; the finite cylinder in a thin boundary layer behaves similarly for 2.5 ≤ AR ≤ 5. Third, for AR > 8, $C_D$ begins to slowly increase with AR. This noticeable change in the behaviour of $C_D$ at higher aspect ratios (starting at AR ≈ 8) for the finite square prism $C_D$ data in the present study) is also seen in the $C_D$ data for finite cylinders in thin boundary layers (Fig. 6(a)) (Beitel *et al*. 2019), but earlier at AR ≈ 5, where it is attributed to changes in size, strength and influence of the near-wake vortex structures.

Increasing the boundary layer thickness tends to lower $C_D$. The data for the thick boundary layer show only two trends. First, there is a rapid increase in $C_D$ with AR for AR ≤ 4.5. The rate of increase in $C_D$ with AR is higher than that of the thin boundary layer and the upper limit moves to AR ≈ 4.5; the same trends are seen in the finite cylinder data. Second, for AR ≥ 4.5, $C_D$ does not attain a constant value but rather slowly increases with AR over the remaining range of aspect ratio tested in the present experiments. This same behaviour is seen for finite cylinders in thick boundary layers (Fig. 6(a)) (Beitel *et al*. 2019). The results suggest that the critical aspect ratios (based on the upper limit of the rapid increase in $C_D$ with AR) are AR ≈ 4 and AR ≈ 4.5 for the thin and thick boundary layers, respectively.

### *4.2 Strouhal number*

Fig. 6(b) shows the behaviour of the Strouhal number at $\alpha = 0°$. At the lowest aspect ratios, for AR ≤ 1.5 for the thin boundary layer and for AR ≤ 2.5 for the thick boundary layer, it was difficult to identify a vortex shedding peak in the power spectrum because the peak was either very broad-banded or absent. These aspect ratios correspond to regime R0 from Porteous *et al*. (2017). Discernable vortex shedding peaks were identified only for AR ≥ 1.5 for the thin boundary layer and for AR ≥ 2.5 for the thick boundary layer. Multiple peaks were not identified in any of the spectra and therefore the St data for 1.5 ≤ AR ≤ 11 for the thin boundary layer and for 2.5 ≤ AR ≤ 11 for the thick boundary layer correspond to regime R1 and peak P1 from Porteous *et al*. (2017).

For both boundary layers, the Strouhal number shows the two distinct trends identified earlier in Fig. 3(b). First, at low aspect ratios (AR ≤ 2.5 for the thin boundary layer, and AR ≤ 5 for the thick boundary layer), St slowly increases with AR. Thereafter, for further increases in AR, the Strouhal number attains a nearly constant value of St ≈ 0.104 up to the maximum aspect ratio tested (AR = 11),

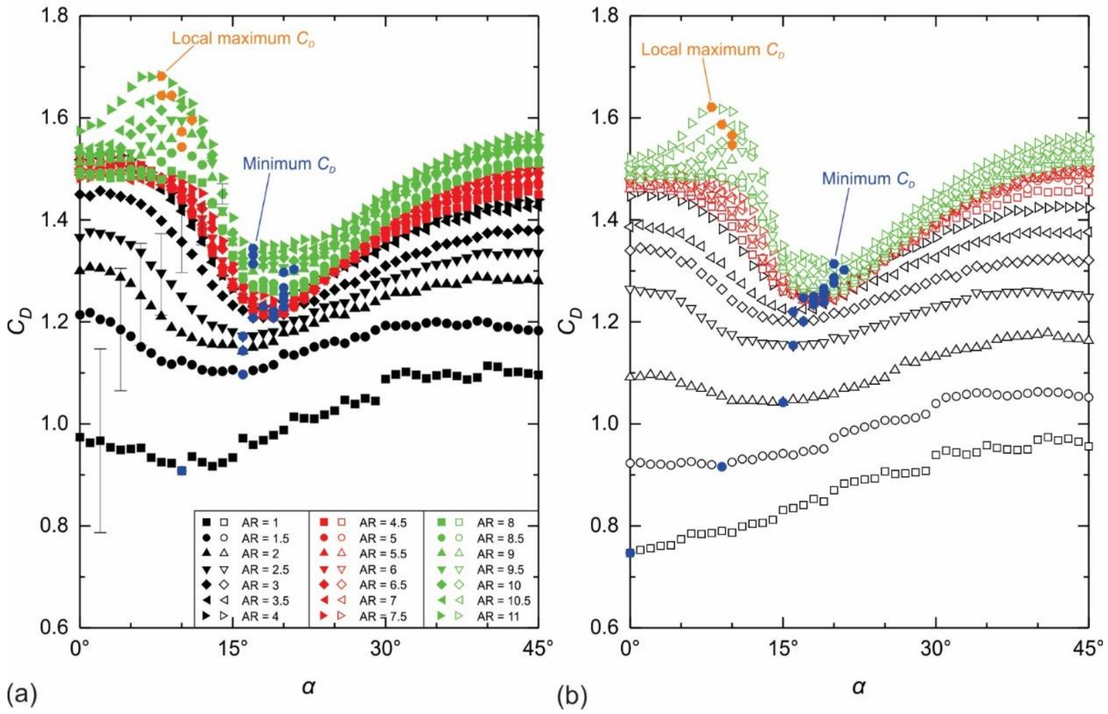


Fig. 7 Mean drag coefficient as a function of incidence angle, Re = 1.1×10$^5$: (a) thin boundary layer ($\delta/D$ = 0.8); (b) thick boundary layer ($\delta/D$ = 2.0). Blue solid circles (●) show locations of minimum $C_D$. Orange solid circles (●) show locations of local maximum $C_D$. Selected error bars shown in (a) to illustrate the uncertainty in the $C_D$ data

with the same value of St obtained for both the thin and thick boundary layers. The present results suggest that an increase in boundary layer thickness mainly acts to delay the onset of vortex shedding to higher AR but otherwise has little influence on the frequency itself. This result is consistent with the general conclusions of the finite square prism studies of Sakamoto and Oiwake (1984), Wang *et al*. (2017), and Kindree *et al*. (2018), but is in contrast to the finite cylinder data (shown in Fig. 6(b)), where the effects of $\delta/D$ are more pronounced.

## 5. Results and discussion (effects of $\alpha$)

The combined effects of incidence angle, aspect ratio, and boundary layer thickness on $C_D$, $C_L$, and St are shown in Figs. 7, 8, and 9, respectively. The present data behave similarly to the data from McClean and Sumner (2014) shown in Fig. 4, but the range of AR is larger and the AR increment is smaller in the present study.

### *5.1 Mean drag force coefficient*

Figure 7 shows the $C_D(\alpha)$ curves for the different aspect ratios and for both boundary layers. A general trend for the mean drag coefficient, for all incidence angles and for both boundary layers, is that $C_D$ increases with AR. The critical incidence angle ($\alpha_c$) corresponding to the minimum $C_D$ (denoted by the solid blue circles in Fig. 7) behaves rather irregularly with AR, mainly because of the difficulty of accurately identifying the minimum, and ranges from $\alpha_c$ = 16° ± 8° at AR = 2 to $\alpha_c$ = 21° ± 4° for AR = 9.5.

In the thin boundary layer (Fig. 7(a)), from AR = 1 to 3.5, the $C_D(\alpha)$ curves change dramatically with AR, both in the magnitude of $C_D$ and the location of $\alpha_c$. These prisms lie below the critical aspect ratio and are therefore strongly influenced by the boundary layer on the ground plane.

From AR = 3.5 to 8, for the thin boundary layer (Fig. 7(a)), there is less variation in the $C_D(\alpha)$ curve with aspect ratio. This range of aspect ratio is similar to that identified in $C_D$(AR) curve for $\alpha$ = 0° in Fig. 6(a), where $C_D$ tended to be unaffected by or be nearly independent of AR. For AR = 8 to 11, the local maximum $C_D$ develops at low incidence angles (identified by the solid orange circles in Fig. 7). This feature is unique to finite-height square prisms (it is absent from 2D square prism $C_D(\alpha)$ curves, Fig. 4(a)) and is therefore related to the finite-prism flow field. The tendency is for the local maximum drag to shift to lower incidence angles as AR is increased.

The main effect of increasing $\delta/D$ is a downward shift in the $C_D(\alpha)$ curves. For AR = 1 to 4.5, where the boundary layer effects are strongest, the curves change dramatically with AR. The prisms of AR = 1 and 1.5 have unique $C_D(\alpha)$ curves without an easily identifiable critical incidence angle and minimum drag. For AR = 4.5 to 8.5, the curves are relatively similar and somewhat independent of AR. For AR = 9 to 11, development of local maximum drag peak is observed. For the thick boundary layer, the critical incidence angle increases with AR and ranges from $\alpha_c$ = 16° ± 6° for AR = 3.5 to $\alpha_c$ = 21° ± 3° for AR = 10.5.

### *5.2 Mean lift force coefficient*

The lift coefficient data for the two boundary layers are

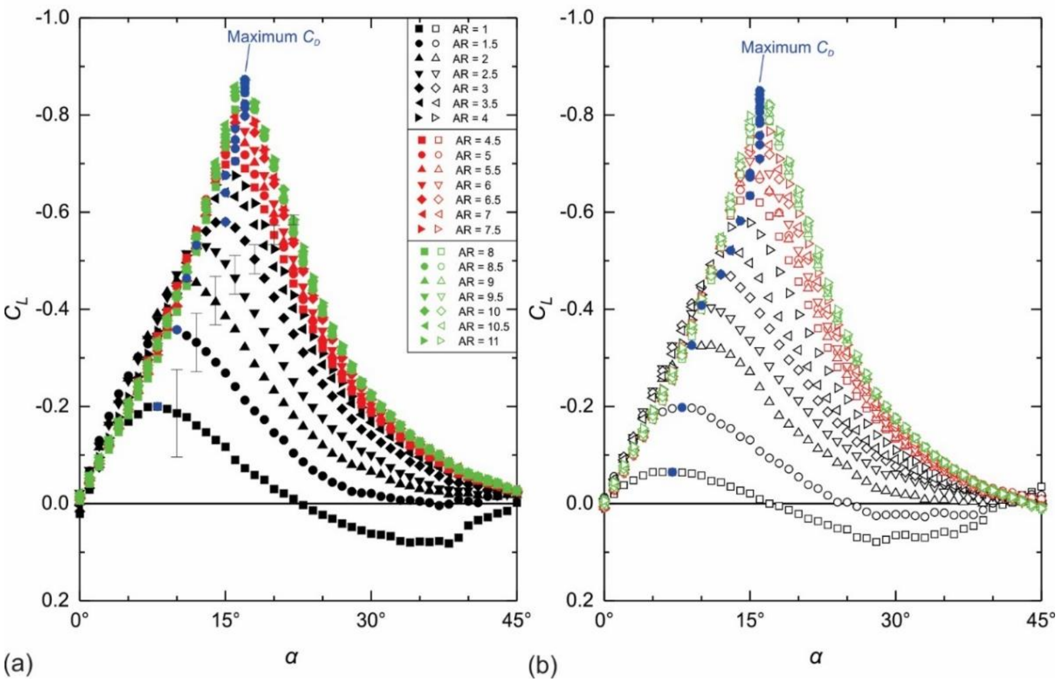


Fig. 8 Mean lift coefficient as a function of incidence angle, Re = 1.1×10$^5$: (a) thin boundary layer ($\delta/D$ = 0.8); (b) thick boundary layer ($\delta/D$ = 2.0). Blue solid circles (●) show locations of maximum $C_L$. Selected error bars shown in (a) to illustrate the uncertainty in the $C_L$ data.

shown in Fig. 8. For the thin boundary layer (Fig. 8(a)), only the prism of AR = 1 experiences a positive mean lift coefficient, from 23° < $\alpha$ < 45°; for all the other aspect ratios $C_L$ is negative. The maximum (most negative) value of lift at the critical incidence angle becomes larger (more negative) as AR increases. The critical incidence angle also increases with AR, and ranges from $\alpha_c$ = 10° ± 4° for AR = 1.5 to $\alpha_c$ = 17° ± 1° for AR = 11. For $\alpha < \alpha_c$, the $C_L(\alpha)$ curves for all aspect ratios and both boundary layers tend to collapse onto a common curve for $\alpha < \alpha_c$, with a "lift slope" of $dC_L/d\alpha = -0.045$ deg$^{-1}$ ± 0.009 deg$^{-1}$. This result suggests that from the perspective of the lateral pressure distribution acting on the sides of the prism, the perfect separation (asymmetric) flow pattern is substantially similar for all prisms (this is in contrast to $C_D(\alpha)$, Fig. 7, which is strongly sensitive to AR in this range of $\alpha$). The strongest effects of AR on the $C_L(\alpha)$ curves are seen for the prisms of AR = 1 to 3.5, and particularly for $\alpha > \alpha_c$. For AR = 8 to 11, the $C_L(\alpha)$ curves become independent of AR and there is no further change in the critical incidence angle.

For the thick boundary layer (Fig. 8(b)), the prisms of AR = 1 and 1.5 experience a positive lift coefficient, and the range of $\alpha$ where it is experienced expands to 17° < $\alpha$ < 45° and 25° < $\alpha$ < 45° for these two aspect ratios, respectively. For the remaining aspect ratios, the behaviour of the $C_L(\alpha)$ curves, the maximum (most negative) lift, and $\alpha_c$ (ranging from $\alpha_c$ = 9° ± 4° for AR = 2 to $\alpha_c$ = 16° ± 1 for AR = 11) are similar to those for the thin boundary layer (Fig. 8(a)). For $\alpha < \alpha_c$, the $C_L$ data collapse to a common curve for all AR; this curve is the same as that of the thin boundary layer, suggesting that boundary layer thickness may not appreciably affect the lift coefficient in the perfect separation (asymmetric) pattern.

### *5.3 Strouhal number*

Strouhal number data are shown in Fig. 9. A Strouhal number for the thin boundary layer case could not be identified (i.e., a peak could not be easily identified in the power spectrum) for the prisms of AR = 1 from $\alpha$ = 0° to 45°, AR = 1.5 from $\alpha$ = 10° to 45°, and AR = 2 from $\alpha$ = 30° to 45°. For the thick boundary layer the peaks were absent for all prisms with AR ≤ 2 from $\alpha$ = 0° to 45° and AR = 2.5 from $\alpha$ = 20° to 45°. Vortex shedding tended to be weaker for the lowest-AR prisms, particularly at higher $\alpha$, and this results in the scatter in the St data in Fig. 9; this finding is similar to the study of Sakamoto (1985) that could not identify vortex shedding frequencies for prisms with AR ≤ 3, especially at a higher incidence angles.

For all aspect ratios, a maximum Strouhal number occurs at a critical incidence angle; for both boundary layers, the general trend is for $\alpha_c$ to increase with AR. For the thin boundary layer, the critical incidence angle ranges from $\alpha_c$ = 15° ± 3° at AR = 2.5 to $\alpha_c$ = 18° ± 1° at AR = 11. For the thick boundary layer, the critical incidence angle ranges from $\alpha_c$ = 11° ± 1° at AR = 2.5 to 17° ± 1° at AR = 11. These ranges of $\alpha_c$ are similar to those identified for minimum $C_D$ and maximum $C_L$ and are higher than those identified for 2D (infinite) square prisms.

There is also a tendency at low incidence angles ($\alpha$ < 15°) and high incidence angles ($\alpha$ > 30°) for an increase in AR to decrease the value of St. This contrasts with the range of incidence angles centred on $\alpha_c$ where it can be seen that increasing AR is associated with an increasing St.

The effect of boundary layer thickness on the Strouhal number data is relatively small, apart from the suppression of vortex shedding peaks at lower AR noted above.

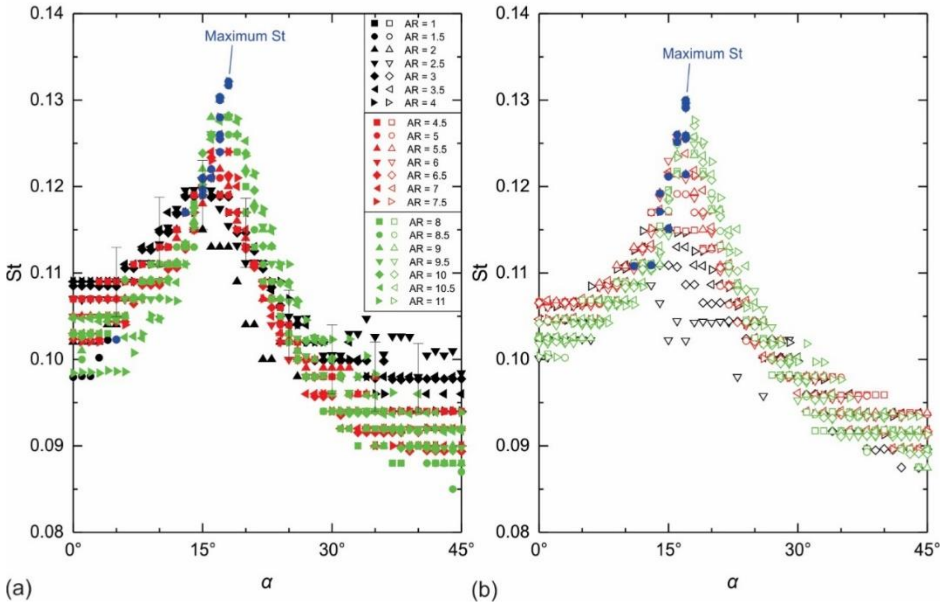


Fig. 9. Strouhal number as a function of incidence angle, Re = $6.5\times10^4$: (a) thin boundary layer ($\delta/D$ = 0.8); (b) thick boundary layer ($\delta/D$ = 2.2). Blue solid circles (●) show locations of maximum St. Selected error bars shown in (a) for the case of AR = 3 to illustrate the uncertainty in St.

However, from comparing Figs. 9(a) and 9(b), it can be seen that the "spread" of the Strouhal number curves tends to be tighter for the case of the thicker boundary layer (Fig. 9(b)).

### *5.4 Discussion*

The behaviour of the critical incidence angle with prism aspect ratio, for minimum $C_D$, maximum $C_L$, and maximum St, is summarised in Fig. 10. The general trend is for the critical incidence angle to increase with aspect ratio up to AR ≈ 6.5 and thereafter attain a constant value (that is higher than that of the 2D prism). Increasing the boundary layer thickness from $\delta/D$ = 0.8 to $\delta/D$ = 2.0-2.2 does not significantly influence the critical incidence angle.

The critical incidence angle data for minimum $C_D$ (Fig. 10(a)) show the largest scatter owing to the difficulty of accurately finding the minimum within the experimental uncertainty, attaining a constant value of $\alpha_c$ = 19° ± 3° for both boundary layer thicknesses. The results for maximum $C_L$ (Fig. 10(b)) and maximum St (Fig. 10(c)) have less uncertainty: for lift, the critical incidence angle attains a constant value of $\alpha_c$ = 17° ± 1° for the thin boundary layer and $\alpha_c$ = 16° ± 1° for the thick boundary layer; for Strouhal number, the values are $\alpha_c$ = 17° ± 1° for both boundary layers. There is therefore general agreement in the $\alpha_c$ value for minimum $C_D$, maximum $C_L$, and maximum St, within the limits of measurement uncertainty, and that $\alpha_c$ is not appreciably influenced by boundary layer thickness (in the range covered in the present experiments).

The data in Fig. 10 show that the critical incidence angle for the finite prism remains higher than the value for the infinite (2D) prism, at least up to AR = 11, and does not show any tendency of converging towards the infinite-prism value. This result, that AR = 11 is not a sufficiently high AR for infinite-prism behaviour, is supported by the study of Porteous *et al*. (2017), for example, who showed that the overall sound pressure level of a finite prism was still lower than the infinite-prism value even at AR = 22.9. A study of finite prisms up to AR = 21.5 by Yauwenas *et al*. (2019) shows that key differences persist in the wakes of finite prisms compared to infinite prisms, such as the cellular vortex shedding phenomenon, that may have an impact on $\alpha_c$. Also, Fox and West (1993) reported that for a finite cylinder, the influence of the free end can extend up to 20 diameters along the cylinder span. Taken together, these studies suggest that convergence of $\alpha_c$ to the value of the infinite prism will not happen until much higher aspect ratios.

The above results suggest that a single flow pattern may be experienced by the prism at $\alpha = \alpha_c$ = 18° ± 2° that brings about a condition of minimum drag, maximum lift, and maximum Strouhal number, at least for intermediate and higher aspect ratios (AR > 3.5 for the thin boundary layer and AR > 4 for the thick boundary layer). This flow pattern occurs at the boundary between the perfect separation (asymmetric) flow pattern (Fig. 2(b)) and the reattachment flow pattern (Fig. 2(c)), where there is the first instance of shear layer reattachment onto trailing edge corner 'c'.

The exact nature of this flow pattern for a finite prism has not yet been clearly described in the literature, however there are some relevant details available in the study of Okuda and Taniike (1993) for a finite prism of AR = 4 (Re = $1.5\times10^4$, $\delta/D$ = 0.36, 2.08, and 6.84). First, a "local extreme suction" (location of large negative mean pressure coefficient) occurs on the upper part of side 'c-d' near corner 'd' for $\alpha$ = 13° to 15° (i.e., the critical incidence angle). This small region of extreme suction is associated with a "standing conical vortex" on the upper part of side 'c-d' of the prism, which forms as the shear layer from

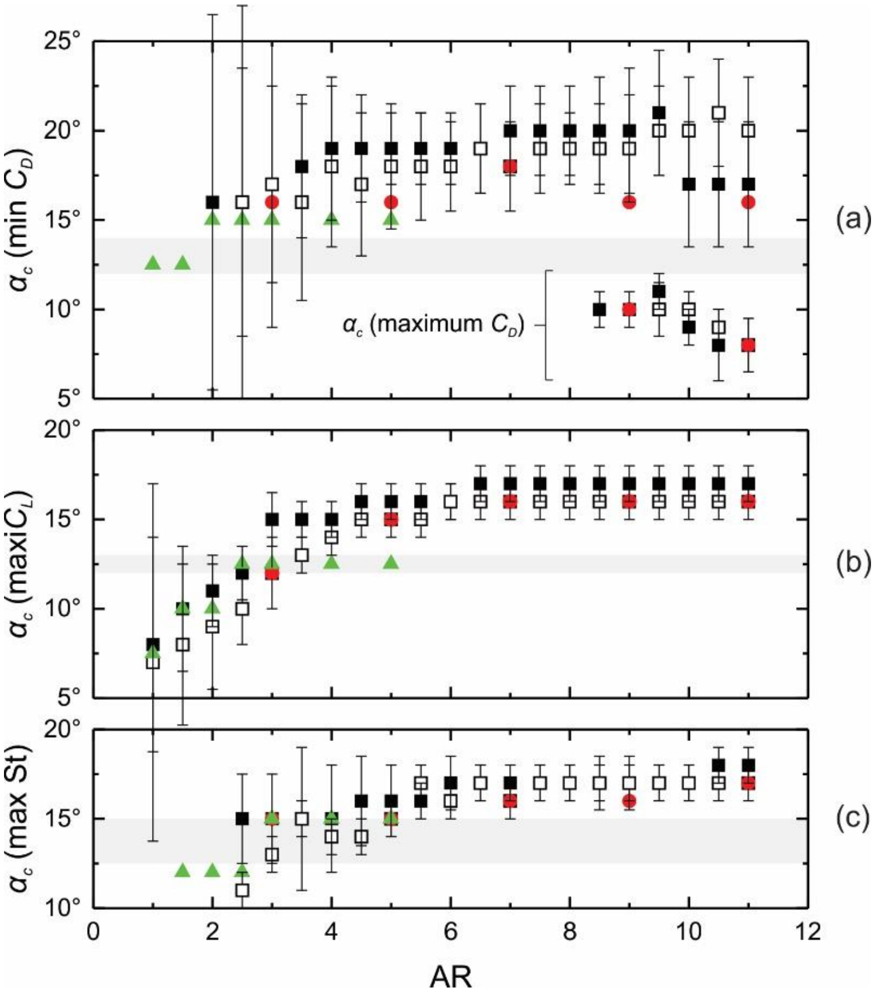


Fig. 10 Behaviour of the critical incidence angle ($\alpha_c$) with prism aspect ratio, based on (a) minimum $C_D$ (Re = 1.1×10$^5$), (b) maximum (most negative) $C_L$ (Re = 1.1×10$^5$), and (c) maximum St (Re = 6.5×10$^4$): ■, thin boundary layer ($\delta/D$ = 0.8); □, thick boundary layer ($\delta/D$ = 2.0 or 2.2); ●, McClean and Sumner (2014), Re = 7.3×10$^4$, $\delta/D$ = 1.5; ▲, Sakamoto (1985), Re = 3.5×10$^4$ to 1.8×10$^5$, $\delta/D$ = 0.67 to 3.33. Grey-shaded region denotes the range of $\alpha_c$ reported in the studies of 2D (infinite) square prisms plotted in Fig. 4.

Table 1. Summary of flow regimes for a surface-mounted finite-height square prism based on aspect ratio

| Regime | Range of AR | Features |
|---|---|---|
| 1 | AR ≈ 1 to 3.5 for thin boundary layer<br>AR ≈ 1 to 4.5 for thick boundary layer | • Regime ends at the critical aspect ratio (AR ≈ 3.5 for the thin boundary layer, AR ≈ 4.5 for the thick boundary layer)<br>• $C_D$, $C_L$, and St increase with AR for all $\alpha$<br>• Absence of discernable St for low $\alpha$<br>• $\alpha_c$ increases with AR<br>• Approximately corresponds to regime R0 from Porteous *et al*. (2017) |
| 2 | AR ≈ 3.5 to 8 for thin boundary layer<br>AR ≈ 4.5 to 8.5 for thick boundary layer | • $C_D$, $C_L$, and St insensitive to changes in AR, particularly for $\alpha < \alpha_c$ and the thick boundary layer<br>• $\alpha_c$ increases with AR until converging to and attaining its final value of = $\alpha_c$ = 18° ± 2°<br>• Approximately corresponds to regime R1 from Porteous *et al*. (2017) |
| 3 | AR ≈ 8 to 11 for thin boundary layer<br>AR ≈ 8.5 to 11 for thick boundary layer | • $C_D$ and $C_L$ slowly increase with AR for low $\alpha$ and the thin boundary layer<br>• $\alpha_c$ independent of AR and boundary layer thickness<br>• Local maximum $C_D$ is observed at $\alpha$ = 8 ± 2° to 11° ± 1°<br>• Approximately corresponds to the end of regime R1 and the start of regime R2 from Porteous *et al*. (2017) |

vertical edge ‘d’ rolls up and reattaches. There is complex interaction between the standing conical vortex and the conical (delta-wing) vortex forming above the free end due to separation from edge ‘c-d’. Second, the reattachment of the shear layer linked to the standing conical vortex is shown to occur on the surface of the prism near the free end, and not on vertical edge ‘c’. The curvature of the reattachment line, however, indicates that reattachment will eventually occur at vertical edge ‘c’ farther down the prism height from the free end. This conjecture is supported by the “bow-shaped” pressure coefficient contours on side ‘c-d’ of the prism, denoting a narrow region of strong adverse pressure gradient; this gradient is strongest for $\alpha$ = 13° to 15° (i.e., the critical incidence angle). The curvature of these pressure contours towards the upstream direction, near the free end and near the ground plane, hence the “bow-shaped” appearance, indicates that reattachment of the shear layer on vertical edge ‘c’ only occurs over the central portion of the prism height. Okuda and Taniike (1993) report that the standing conical vortex appears only near $\alpha_c$; its behaviour has not been extensively studied otherwise.

Additional insight into the flow pattern at $\alpha = \alpha_c$ by Unnikrishnan *et al*. (2017) shows the prism has its shortest mean recirculation zone and highest asymmetry in its mean wake. This asymmetry appears as a shift of the wake away from centreline (in the $+y$ direction), deflection of the downwash (in the $+y$ direction), and changes in the relative sizes, locations, and strengths of the tip vortices; the relative sizes of the tip vortices in the upper part of the wake are linked to the different sizes of the conical (delta-wing) vortices originating from edges ‘a-b’ and ‘c-d’ on the free end.

The general behaviour of $C_D$, $C_L$, and St with AR suggests the existence of three possible flow regimes (Table 1). The first flow regime occurs at low aspect ratios (AR ≈ 1 to 3.5 for the thin boundary layer, AR ≈ 1 to 4.5 for the thick boundary layer), when the prism is below the critical aspect ratio and where $C_D$, $C_L$, and St increase with AR. This increase in $C_D$, $C_L$, and St with AR occurs for all incidence angles, not just at $\alpha$ = 0°. This flow regime broadly corresponds to regime R0 from Porteous *et al.* (2017). Although Porteous *et al*. (2017) only considered the case of $\alpha$ = 0° when determining their flow regimes, the results of the present study suggest that regime R0 is also seen for non-zero $\alpha$. Insight into the flow structures for these non-zero $\alpha$ can be found in results for the flow around a cube at incidence (Natarajan and Chyu 1994).

The second flow regime occurs at intermediate aspect ratios (AR ≈ 3.5 to 8 for the thin boundary layer, AR ≈ 4.5 to 8.5 for the thick boundary layer) where $C_D$, $C_L$, and St are less sensitive to changes in $\alpha$, in particular for $\alpha < \alpha_c$ and for thick boundary layers. The critical incidence angle continues to increase with AR but converges to and attains its final value within this range of AR.

The third flow regime is found at higher aspect ratios (AR ≈ 8 to 11 for the thin boundary layer, AR ≈ 8.5 to 11 for the thick boundary layer), where $C_D$ and $C_L$ slowly increase with AR for low incidence angles and the thin boundary layer. The local maximum $C_D$ is also found in this flow regime (Fig. 10(a)), at an incidence angle ranging from $\alpha$ = 8 ± 2° (at AR = 11) to 11° ± 1° (at AR = 8), which places this phenomenon within the perfect separation (asymmetric) flow pattern (Fig. 2(b)). The critical incidence angle for minimum $C_D$, maximum $C_L$, and maximum St, remains constant in the third flow regime. This flow regime would correspond to the end of the regime R1 and the start of regime R2 based on Porteous *et al*. (2017).

For all three regimes, the behaviour of the “inverted conical vortex” (Okuda and Taniike 1993) on side ‘c-d’ and the conical (delta-wing) vortices above the free end with changes in AR and $\alpha$ is key to an eventual physical interpretation of the $C_D$, $C_L$, and St data. To date, however, there has been limited systematic exploration of these flow for surface-mounted finite-height square prisms.

## 6. Conclusions

The behaviour of $C_D$, $C_L$, and St was examined for the flow around a surface-mounted, finite-height square prism, with a focus on the effects of AR, $\alpha$, and $\delta/D$. Wind tunnel experiments were conducted at Re = $6.5\times10^4$ and $1.1\times10^5$ for two boundary layer conditions: a thin boundary layer with $\delta/D$ = 0.8 and a thick boundary layer with $\delta/D$ = 2.0–2.2. The aspect ratio was varied from AR = 1 to 11 in increments of 0.5 and the incidence angle was varied from $\alpha$ = 0° to 45° in increments of 1°. The main conclusions of the study are summarized below:

- $C_D$ is a strong function of AR, $\alpha$, and $\delta/D$. The minimum $C_D$ occurs at a critical incidence angle $\alpha_c$ that varies with AR. At high aspect ratios, a local maximum $C_D$ occurs at $\alpha$ = 8° ± 2° to 11° ± 1° that is not observed for the infinite (2D) square prism.
- $C_L$ is a strong function of AR, $\alpha$, and $\delta/D$. Its behaviour is similar to the infinite (2D) square prism. The maximum $C_L$ occurs at $\alpha_c$ that varies with AR. Positive lift coefficients are experienced at high $\alpha$ only by finite prisms of very low aspect ratio; otherwise, finite prisms experience only negative lift coefficients, which is in contrast to $C_L$ data for infinite prisms. The “lift slope” $dC_L/d\alpha$ for $\alpha < \alpha_c$ is similar for all AR and both values of $\delta/D$.
- St is a strong function of $\alpha$ but is less sensitive to AR and $\delta/D$ compared to $C_D$ and $C_L$. Its behaviour is similar to the 2D square prism. The maximum St occurs at $\alpha_c$ that varies with AR. For small AR, vortex shedding is weak or absent for all or a limited range of $\alpha$.
- There is a single value of $\alpha_c$ at which the prism experiences its minimum $C_D$, maximum (most negative) $C_L$, and maximum St. The value of $\alpha_c$ increases with AR and reaches a terminal value of $\alpha_c$ = 18° ± 2° once AR is sufficiently high (AR ≥ 8). This terminal value of $\alpha_c$ for higher-aspect ratio finite prisms is higher than that of infinite (2D) square prisms. The critical incidence angle is insensitive to $\delta/D$ for the values examined in this study.
- The behaviour of $C_D$, $C_L$, and St with AR suggest the possibility of three flow regimes. The specific flow patterns responsible for the behaviour of $C_D$, $C_L$, and St for surface-mounted finite-height prisms at different AR, $\alpha$, and $\delta/D$ have not been extensively studied to date; a physical interpretation will require a better understanding of the conical (delta-wing) vortices originating along leading edges of the free end, the

nature of the reattachment on the side of the prism, the inverted conical vortex on the side of the prism, the standing conical vortex on the side of the prism at $\alpha = \alpha_c$, the mutual interaction of these structures, and how these flow features interact with the more widely studied (at $\alpha = 0°$) vortex dynamics of the near wake.

## Acknowledgments

Financial support from the NSERC Discovery Grants program (Grant No. 2018-03760), the College of Engineering's Graduate Research Fellowship program, and the Department of Mechanical Engineering's Graduate Scholarships program, is gratefully acknowledged. The technical assistance of Shawn Reinink, Rob Peace, and Engineering Shops is also recognized.

## References

Akins, R.E., Peterka, J.A. and Cermak, J.E. (1977), "Mean force and moment coefficients for buildings in turbulent boundary-layers", *J Wind Eng. Ind Aerod*., **2**(3), 195-209. https://doi.org/10.1016/0167-6105(77)90022-8.

Bai, H.L. and Alam, M.M. (2018), "Dependence of square cylinder wake on Reynolds number", *Phys Fluids*, **30**(1), 015102. https://doi.org/10.1063/1.4996945.

Behera, S. and Saha, A.K. (2019), "Characteristics of the flow past a wall-mounted finite-length square cylinder at low Reynolds number with varying boundary layer thickness", *J. Fluid Eng*. **141**(6), https://doi.org/10.1115/1.4042751.

Beitel, A., Heng, H. and Sumner, D. (2019), "The effect of aspect ratio on the aerodynamic forces and bending moment for a surface-mounted finite-height cylinder", *J Wind Eng. Ind. Aerod*., **186**, 204-213. https://doi.org/10.1016/j.jweia.2019.01.009.

Cao, Y., Tamura, T. and Kawai, H. (2019), "Investigation of wall pressures and surface flow patterns on a wall-mounted square cylinder using very high-resolution Cartesian mesh", *J. Wind Eng. Ind. Aerod*., **188**, 1-18. https://doi.org/10.1016/j.jweia.2019.02.013.

El Hassan, M., Bourgeois, J. and Martinuzzi, R. (2015), "Boundary layer effect on the vortex shedding of wall-mounted rectangular cylinder", *Exp Fluids*, **56**(2), https://doi.org/10.1007/s00348-014-1882-6.

Fox, T.A. and West, G.S. (1993), "Fluid-induced loading of cantilevered circular cylinders in a low-turbulence uniform flow. Part 1: Mean loading with aspect ratios in the range 4 to 30", *J. Fluid Struct*., **7**(1), 1-14. https://doi.org/10.1006/jfls.1993.1001.

Hosseini, Z., Bourgeois, J.A. and Martinuzzi, R.J. (2013), "Large-scale structures in dipole and quadrupole wakes of a wall-mounted finite rectangular cylinder", *Exp Fluids*, **54**(9). https://doi.org/10.1007/s00348-013-1595-2.

Igarashi, T. (1984), "Characteristics of the flow around a square prism", *B JSME*, **27**(231), 1858-1865. https://doi.org/10.1299/jsme1958.27.1858.

Kindree, M.G., Shahroodi, M. and Martinuzzi, R.J. (2018), "Low-frequency dynamics in the turbulent wake of cantilevered square and circular cylinders protruding a thin laminar boundary layer", *Exp Fluids*, **59**(12), 186. https://doi.org/10.1007/s00348-018-2641-x.

Knisely, C.W. (1990), "Strouhal numbers of rectangular cylinders at incidence - a review and new data", *J. Fluid Struct*., **4**(4), 371-393.

Lee, B.E. (1975), "The effect of turbulence on surface pressure field of a square prism", *J Fluid Mech*., **69**(2), 263-282.

Lee, Y.T., Boo, S.I., Lim, H.C. and Misutani, K. (2016), "Pressure distribution on rectangular buildings with changes in aspect ratio and wind direction", *Wind Struct*, **23**(5), 465-483. http://dx.doi.org/10.12989/was.2016.23.5.465.

Lim, H.C. (2009), "Wind flow around rectangular obstacles with aspect ratio", *Wind Struct*, **12**(4), 299-312. https://doi.org/10.12989/was.2009.12.4.299.

McClean, J.F. and Sumner, D. (2014), "An experimental investigation of aspect ratio and incidence angle effects for the flow around surface-mounted finite-height square prisms", *J Fluid Eng*., **136**(8). https://doi.org/10.1115/1.4027138.

Moreau, D.J. and Doolan, C.J. (2013), "Flow-induced sound of wall-mounted finite length cylinders", *AIAA J*., **51**(10), 2493-2502. https://doi.org/10.2514/1.J052391.

Natarajan, V. and Chyu, M.K. (1994), "Effect of flow angle-of-attack on the local heat mass-transfer from a wall-mounted cube", *J Heat Trans*., **116**(3), 552-560. https://doi.org/10.1115/1.2910906.

Norberg, C. (1993), "Flow around rectangular cylinders - pressure forces and wake frequencies". *J. Wind Eng. Ind. Aerod*., **49**(1-3), 187-196. https://doi.org/10.1016/0167-6105(93)90014-F.

Obasaju, E.D. (1983), "An investigation of the effects of incidence on the flow around a square section cylinder", *Aeronaut Quart*, **34**(4), 243-259. https://doi.org/10.1017/S0001925900009768.

Okuda, Y. and Taniike, Y. (1993), "Conical vortices over side face of a three-dimensional square prism", *J. Wind Eng. Ind. Aerod*., **50**, 163-172. https://doi.org/10.1016/0167-6105(93)90071-U.

Porteous, R., Moreau, D.J. and Doolan, C.J. (2017), "The aeroacoustics of finite wall-mounted square cylinders", *J. Fluid Mech*., **832**, 287-328. https://doi.org/10.1017/jfm.2017.682.

Saha, A.K. (2013), "Unsteady flow past a finite square cylinder mounted on a wall at low Reynolds number", *Comput. Fluids*, **88**(15), 599-615. https://doi.org/10.1016/j.compfluid.2013.10.010.

Sakamoto, H. (1985), "Aerodynamic forces acting on a rectangular prism placed vertically in a turbulent boundary-layer", *J. Wind Eng. Ind. Aerod*., **18**(2), 131-151. https://doi.org/10.1016/0167-6105(85)90093-5.

Sakamoto, H. and Arie, M. (1983), "Vortex shedding from a rectangular prism and a circular-cylinder placed vertically in a turbulent boundary-layer", *J. Fluid Mech*., **126**, 147-165. https://doi.org/10.1017/S0022112083000087.

Sakamoto, H. and Oiwake, S. (1984), "Fluctuating forces on a rectangular prism and a circular-cylinder placed vertically in a turbulent boundary-layer", *J. Fluid Eng. Trans*., **106**(2), 160-166. https://doi.org/10.1115/1.3243093.

Sarode, R.S., Gai, S.L. and Ramesh, C.K. (1981), "Flow around circular-section and square-section models of finite height in a turbulent shear-flow", *J. Wind Eng. Ind. Aerod*., **8**(3), 223-230. https://doi.org/10.1016/0167-6105(81)90022-2.

Sohankar, A., Esfeh, M.K., Pourjafari, H., Alam, M.M. and Wang, L.J. (2018), "Features of the flow over a finite length square prism on a wall at various incidence angles", *Wind Struct*, **26**(5), 317-329. https://doi.org/10.12989/was.2018.26.5.317.

Sumner, D., Rostamy, N., Bergstrom, D.J. and Bugg, J.D. (2017), "Influence of aspect ratio on the mean flow field of a surface-mounted finite-height square prism", *Int. J. Heat Fluid Flow*, **65**, 1-20. https://doi.org/10.1016/j.ijheatfluidflow.2017.02.004.

Unnikrishnan, S., Ogunremi, A. and Sumner, D. (2017), "The effect of incidence angle on the mean wake of surface-mounted finite-height square prisms", *Int J Heat Fluid Fl*, **66**, 137-156. https://doi.org/10.1016/j.ijheatfluidflow.2017.05.012

Wang, H., Zhou, Y., Chan, C. and Zhou, T. (2009), "Momentum and heat transport in a finite-length cylinder wake", *Exp Fluids*, **46**(6), 1173-1185. https://doi.org/10.1007/s00348-009-0620-y.

Wang, H.F. and Zhou, Y. (2009), "The finite-length square cylinder near wake", *J. Fluid Mech*., **638**, 453-490. https://doi.org/10.1017/S0022112009990693.
Wang, H.F., Zhao, X.Y., He, X.H. and Yu, Z. (2017), "Effects of oncoming flow conditions on the aerodynamic forces on a cantilevered square cylinder", *J. Fluid Struct*., **75**, 140-157. https://doi.org/10.1016/j.jfluidstructs.2017.09.004.
Wang, H.F., Zhou, Y., Chan, C.K. and Lam, K.S. (2006), "Effect of initial conditions on interaction between a boundary layer and a wall-mounted finite-length-cylinder wake", *Phys*. *Fluids*, **18**(6), 065106. doi:10.1063/1.2212329
Wang, Y.Q. (2019), "Effects of Reynolds number on vortex structure behind a surface-mounted finite square cylinder with AR = 7", *Phys Fluids*, **31**(11), 115103. https://doi.org/10.1063/1.5123994.
Yauwenas, Y., Porteous, R., Moreau, D.J. and Doolan, C.J. (2019), "The effect of aspect ratio on the wake structure of finite wall-mounted square cylinders", *J. Fluid Mech*., **875**, 929-960. https://doi.org/10.1017/jfm.2019.522.
Yen, S.C. and Yang, C.W. (2011), "Flow patterns and vortex shedding behavior behind a square cylinder", *J. Wind Eng. Ind. Aerod*., **99**(8), 868-878. https://doi.org/10.1016/j.jweia.2011.06.006.
Zhang, D., Cheng, L., An, H.W. and Zhao, M. (2017), "Direct numerical simulation of flow around a surface-mounted finite square cylinder at low Reynolds numbers", *Phys Fluids*, **29**(4), 045101. https://doi.org/10.1063/1.4979479.

*CC*